Standardized cycle life assessment of batteries using extremely lean electrolytic testing conditions

Check for updates

Myeong Gyun Nam[1], Hyun Jun Song[1], Jin Kyo Koo[2], Gwan Hyun Choi[1], Yong Seok Kim[3], Hye Jin Kim[3], Chang-Su Shin[3], Youngugk Kim[3], Jae Hou Nah[3], Young-Jun Kim [2,4] & Pil J. Yoo [1,2,4] ✉

Despite the proposal of numerous advanced materials for batteries, there remains a notable lack of comprehensive assessment protocols that facilitate direct comparisons between laboratory-scale research and industrial trials. Here, we introduce a standardized method coined as extremely lean electrolytic testing (ELET), designed as a uniform framework for evaluating the performance across different battery systems. This approach replicates the cycling behaviour of larger pouch cells within the more manageable format of coin cells under ELET conditions. Employing ELET, we develop quantitative models to create contour maps that standardize cell performance metrics. To demonstrate the ELET efficacy, we explore the mitigation of electrolyte decomposition in lithium-ion batteries through applying polydopamine coatings on silicon/carbon composite anodes, achieving a 150% decrease in electrolyte decomposition compared to uncoated ones. Additionally, we employ the ELET method to compare the performance of various post-secondary and commercial batteries, demonstrating its full utility in battery evaluation.

To meet the growing demand for electric devices and vehicles, secondary battery systems centered on lithium (Li), such as Li-ion batteries (LIB) and Li-sulfur batteries, have been developed with the aim of achieving high energy densities. Diverse electrode materials endowed with high capacities have been proposed for these battery platforms. In particular, to enhance energy density, silicon (Si)-based composites such as carbon (C)-coated Si nanoparticles complexes[1,2], prelithiated Si composites[3], and dimension-controlled Si-C composites[4,5] have emerged as a viable alternative to graphite in anodes, while cathodes employ sulfur (sulfur-catalyst[6], sulfur-C[7,8], and sulfur-infused composites[9,10]) or oxygen-based materials (Li_2O_2[11–13] and gaseous O_2[14]). Nevertheless, the use of highly capacitive materials can expedite undesirable side reactions, involving electrolyte decomposition during battery operation, thereby leading to a reduction in the cycle life of the battery system and formation of solid electrolyte interphase (SEI)[15,16] and cathode electrolyte interphase[17] layers on the anode and cathode, respectively. Particularly, Si-based anodes, electrolytic species undergo reduction at low voltages, resulting in the formation of adsorbates like SEI layers on the electrode surface, which hampers the facile transport of Li ions to the active material[18,19]. As the cell undergoes repetitive charge-discharge cycles and the active material experiences volumetric expansion due to lithiation, the

exposed surface area increases, culminating in the accumulation of larger amounts of adsorbates[20,21]. In cathodes, especially within Li metal batteries, electrolytic species can engage in reactions with the lithiated cathodic material via nucleophilic attack[22,23] or high-voltage oxidation[24]. Consequently, as the electrolyte degrades, the concentrations of active components decrease, and the electrochemical activity of the system diminishes, ultimately lowering the overall cell performance.

Furthermore, the progressive deterioration of the electrolyte eventually leads to the failure of the battery cell, imposing severe constraints on the practical deployment of high-capacity battery systems. Despite the development of active materials with high energy densities, a substantial portion of them falls short of meeting the requisite cycle life for industrial use, primarily due to the depletion and decomposition of the electrolyte during cell operation[25–27]. This issue is particularly pronounced in industrial pouch cells, where the amount of electrolyte employed is markedly lower than that in laboratory coin cells, aiming to maximize the battery's energy density for practical purposes. Cell performance, when measured in terms of energy density, takes into account the weight or volume of entire cell components, whereas specific capacity calculations are based solely on active material data. As a result, even if practical and lab-scale cells have identical capacities

[1]School of Chemical Engineering, Sungkyunkwan University (SKKU), Suwon 16419, Republic of Korea. [2]SKKU Advanced Institute of Nanotechnology (SAINT), Sungkyunkwan University (SKKU), Suwon 16419, Republic of Korea. [3]R&D Center, Samsung SDI Co., Ltd, Suwon 16678, Republic of Korea. [4]SKKU Institute of Energy Science and Technology (SIEST), Sungkyunkwan University (SKKU), Suwon 16419, Republic of Korea. ✉e-mail: pjyoo@skku.edu

and cycle life, the performance of a cell operating under practical lean electrolyte conditions is incomparably superior to its lab-scale counterpart. The ideal quantity of electrolytes for practical cells is typically set to match the corresponding pore volume of electrodes and separators, implying that the optimal amount of lean electrolyte is strongly influenced by the properties of these components. Additionally, the practical utilization of lean electrolyte conditions is affected by the electrolyte-wetting properties of electrodes and separators, which determine how well the electrolytes permeate their porous structures. In commercial cells, the electrolyte-to-capacity (E/C) ratio is commonly maintained below $2\,\mu l\,mAh^{-1}$, a remarkably low electrolyte content[28]. Despite its advantages, such lean electrolyte conditions pose challenges for high-capacity battery systems due to exacerbated levels of electrolyte decomposition in post-electrode materials. In particular, insufficient initial Coulombic efficiencies in post-electrode systems make it difficult to effectively reduce the E/C ratio. Moreover, as cycles progress, gradual electrolyte decomposition leads to significantly reduced cycle life of cells. Ultimately, commercial-scale cells can experience abrupt failure due to the depletion of their limited electrolyte supply, with a noticeable capacitive plunge often occurring once the electrolyte is exhausted.

To address this challenge, it is rational to subject cells to testing under lean electrolyte conditions that properly replicate the testing conditions encountered in large-scale pouch cells[29,30]. However, the threshold at which cell failure occurs remains contingent on the electrolyte quantity relative to the overall cell capacity, even under a lean electrolyte environment. This variability renders cell performance insensitive to failure, resulting in challenges in accurately detecting the cell failure threshold and consistently quantifying cell performance, even when utilizing identical samples. These inconsistencies impede precise and quantitative comparisons of cell cycle life and the assessment of their viability in commercial applications. As a result, a considerable number of the methods proposed to improve the cycle life of active materials in LIBs have yet to find practical implementation in cell systems. This reveals a disparity in the effectiveness of proposed methodologies between academic research and industrial trials, highlighting the imperative need for more standardized and advanced measurement conditions and accompanying analytical tools. Therefore, the establishment of standardized criteria that factor in the extent of electrolyte decomposition based on the type of active material could serve as a bridge linking the gap between academic research results and industrial-scale testing, facilitating more reliable comparisons and well-informed decisions in the realms of battery development and application.

In general, the strategies employed to enhance the cycle life of battery systems vary depending on the specific type and constituents of the cells. To mitigate electrolyte decomposition, a prevalent approach involves encapsulating active materials within supportive structures through various coating techniques. For instance, in LIBs, carbon-based materials, renowned for their high elastic moduli and electrical conductivity, have been employed as coatings on the surfaces of Si particles within the anodes. This intervention serves to prevent the pulverization of the active material during the repeated lithiation-delithiation cycles[31,32]. However, it is worth noting that these coatings also function as electrolyte-blocking layers that impede direct contact between the electrolyte and the electrode materials, while simultaneously allowing for the selective passage of Li ions. As such, these blocking layers must exhibit specific characteristics, including selective Li-ion conductivity, excellent insulating properties, and sufficient mechanical durability to effectively shield the active material surface and concurrently suppress the decomposition of the electrolyte. Consequently, this regulation of SEI growth plays a pivotal role in preserving the integrity of the electrolyte and extending the life cycle of the cell.

In this context, polymers incorporating Li-conductive functional groups have emerged as promising candidates for electrolyte-blocking layers[33,34]. Among these, phenolic compounds featuring abundant hydroxyl groups have attracted significant research interest due to their exceptional adhesive properties[35,36] and potent Li-binding capabilities[37–39] inherent in the incorporated functional groups. These attributes render phenolic compounds highly effective in forming coatings and facilitating high Li-ion conductivity on various substrates[40,41]. Among diverse phenolic compounds, dopamine particularly stands out as a pioneering seeding material utilized as a complexing agent. The electron-donating amine group present in dopamine demonstrates remarkable adsorption properties on a wide array of surfaces. Coupled with other types of interactions available, such as hydrogen bonding, van der Waals interactions, and π-interactions, the indole-transformative nature of the amine groups enables uniform adsorption of charges on surfaces regardless of their composition or hydrophilic properties[42]. Hence, the polymerized form of dopamine holds immense potential as a fundamental constituent of electrolyte-blocking layers, even on inert surfaces possessing limited functional groups, such as carbonaceous materials, thanks to its exceptional adsorption and chelation properties. Accordingly, when applied as a coating layer, it serves as an ideal blocking layer while minimally impacting the electrochemical activity of the active material itself. This attribute allows for the generation of optimal comparative samples for evaluating the cycle life characteristics of capacity-stabilizing strategies.

In this study, we propose a comprehensive model for the evaluation of cell cycle life under the rigorous conditions of extremely lean electrolyte testing (ELET) as a means to standardize the assessment of cycle performance in small-scale cells while effectively representing the performance characteristics of large-scale pouch cells. The proposed methodology involves the utilization of a coin cell configuration with an extremely small amount of electrolyte ($<2\,\mu l\,mAh^{-1}$), which can be readily depleted during cycles. This approach allows us to emulate the capacitive plunging behavior observed in pouch cells with capacities spanning a few amperes, even within the confines of smaller-scale coin cells. This, in turn, facilitates meaningful performance comparisons between these two distinct cell types. Additionally, a quantitative mathematical model was developed to gauge standardized cell performance based on data acquired through the ELET methodology. As a result, visually intuitive contour maps were established to analyze ELET performance, effectively mirroring the behavior of pouch cells, albeit within the reduced dimensions of coin cell configurations. Moreover, we applied the ELET technique to explore a spectrum of cell configurations, encompassing commercialized LIB setups and basic configurations of LSB, highlighting its versatility across diverse battery systems. In particular, we have scrutinized the efficacy of mitigating electrolyte decomposition and extending battery cell life by employing polydopamine (PD) layers as coatings on Si-C composites, utilizing the proposed ELET technique. By harnessing the ELET method in conjunction with associated analytical tools, our study endeavors to strengthen the connections between outcomes derived from academic research and those stemming from industrial trials, utilizing quantified evaluation maps. Consequently, this advancement is poised to accelerate the progression of next-generation high-performance battery systems.

Results and discussion
Extremely lean electrolytic testing methodology
Figure 1a depicts the mechanism of inhibiting electrolyte decomposition through the implementation of an electrolyte-blocking layer on the surface of active materials. A substantial portion of electrolyte molecules at the unstable surface of active materials is susceptible to electrochemical decomposition, leading to the consumption of Li ions in the form of a SEI layer. However, when the surface is passivated with a selective Li-ion conducting layer, the likelihood of solvent molecules reacting with the surface decreases. As a result, this approach alleviates the consumption of Li ions from the electrolyte, thereby enabling the cell to sustain a stable capacity. Therefore, the deterioration in capacity can be quantified based on the reaction kinetics of electrolyte decomposition[43]. Utilizing a derived kinetics model, a three-dimensional (3D) contour plot representing cell capacity can be constructed. This plot integrates key variables from established kinetics, including time, rate constant ($R_{f,0}$), and a quantitative indicator of SEI growth denoted as $D\,(\delta/L_0)$, where δ and L_0 are constants proportional to the molar volume and initial thickness of the SEI layer, respectively (Fig. 1b and
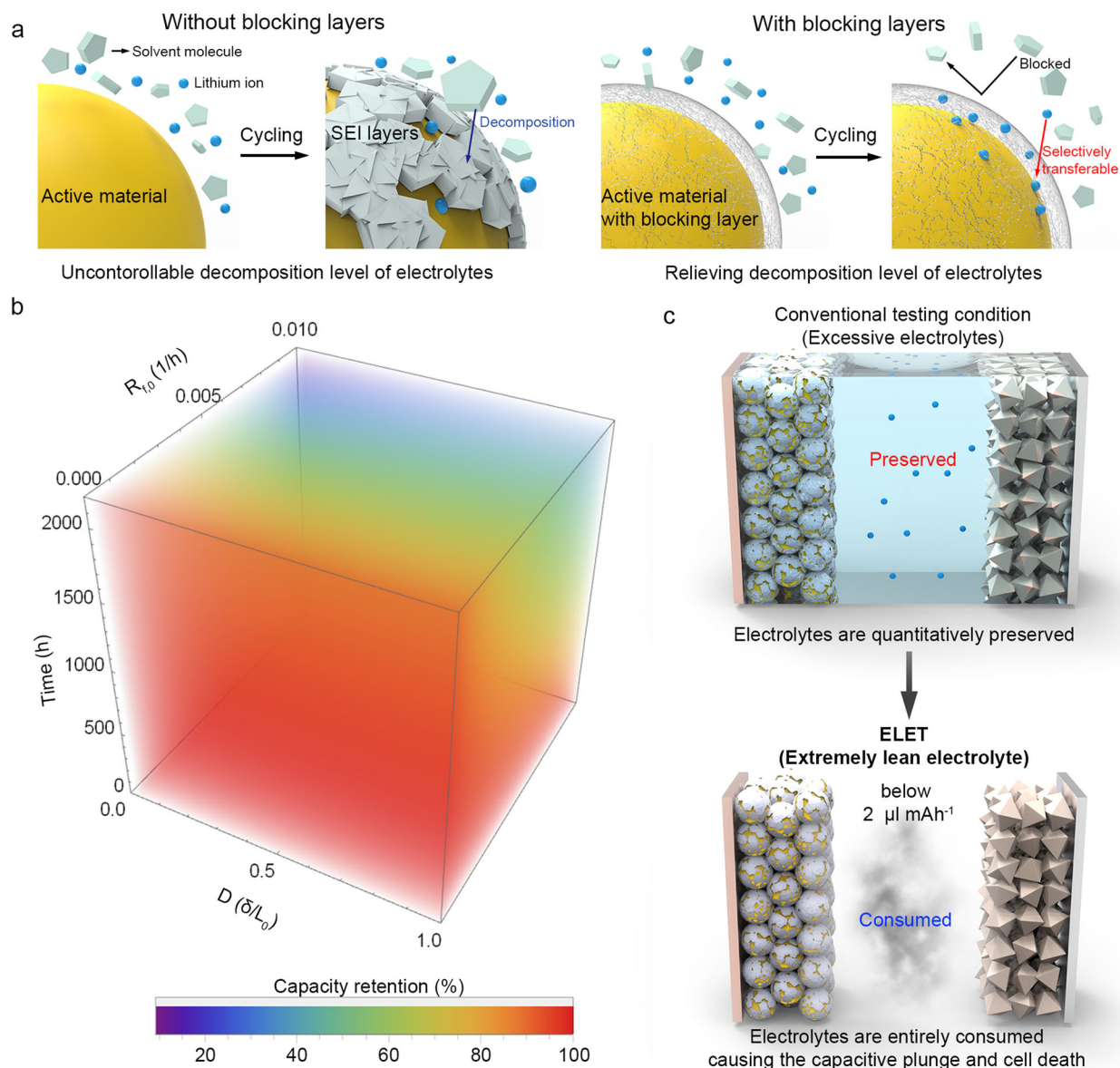
Fig. 1 | Illustrations for the trend of capacity-fading as electrolytes undergo decomposition. a Schematic depicting the mechanism of the inhibition of SEI layer growth through the introduction of the electrolyte-blocking layer coating. **b** 3D contour plot representing capacity retention based on a model derived from the kinetics of SEI formation reactions. **c** Schematic illustrating the observation of electrolyte depletion using the ELET technique for assessing battery cycle life.

Supplementary Note 1). Here, the rate constant and quantitative indicator for SEI growth are material-specific, allowing for the conversion of capacity degradation into terms specific to the active material. In cases where the electrolyte cannot provide additional Li ions during cycling, the cell capacity will decline rapidly in accordance with the contour plot. To determine the actual depletion point of Li ions attributable to electrolyte decomposition within the cell, it is essential to define the conditions under an extremely lean electrolyte employment (Fig. 1c). Once the supply of electrolytic species within the cells is depleted to a level insufficient for cell operation, the dominance of cell failure ensues, resulting in a capacitive plunge in the cell capacity. Therefore, by monitoring and comparing the cycles at which the capacitive plunge occurs under specific cell configurations, a rational model for evaluating the cell performance of various active materials and battery systems can be established.

Characterization of the as-prepared active materials

When comparing the degree of electrolyte decomposition in LIB systems, it is pertinent to employ commonly used commercial materials. Si-C

composites are extensively investigated and employed as anode materials in practical LIB applications, despite their susceptibility to electrolyte decomposition owing to severe volume expansion during battery operation. In this study, we implemented a blocking layer of PD formed through oxidative polymerization on the surface of Si-C composites to mitigate electrolyte decomposition (denoted as Si–C/PD, Supplementary Fig. 1)[44]. Following the coating of PD layers onto the Si-C composites, the presence of these layers was examined using various analytical techniques, including X-ray diffraction (XRD) patterns and imaging analyses conducted through transmission electron microscopy (TEM) and scanning electron microscopy (SEM) (Fig. 2a, 2b and Supplementary Figs. 2–4). Furthermore, energy -dispersive spectroscopic (EDS) elemental maps (Fig. 2c–2f) demonstrated the accumulation of PD layers on the Si-C composite surface after 16 h of polymerization. This process successfully overcame the intrinsic hydrophobic nature of bare Si-C composite surface (Supplementary Fig. 5).

To address the issue of a reduction in electrical resistance that can arise from the thick PD layer, the coating time for the PD layer was optimized
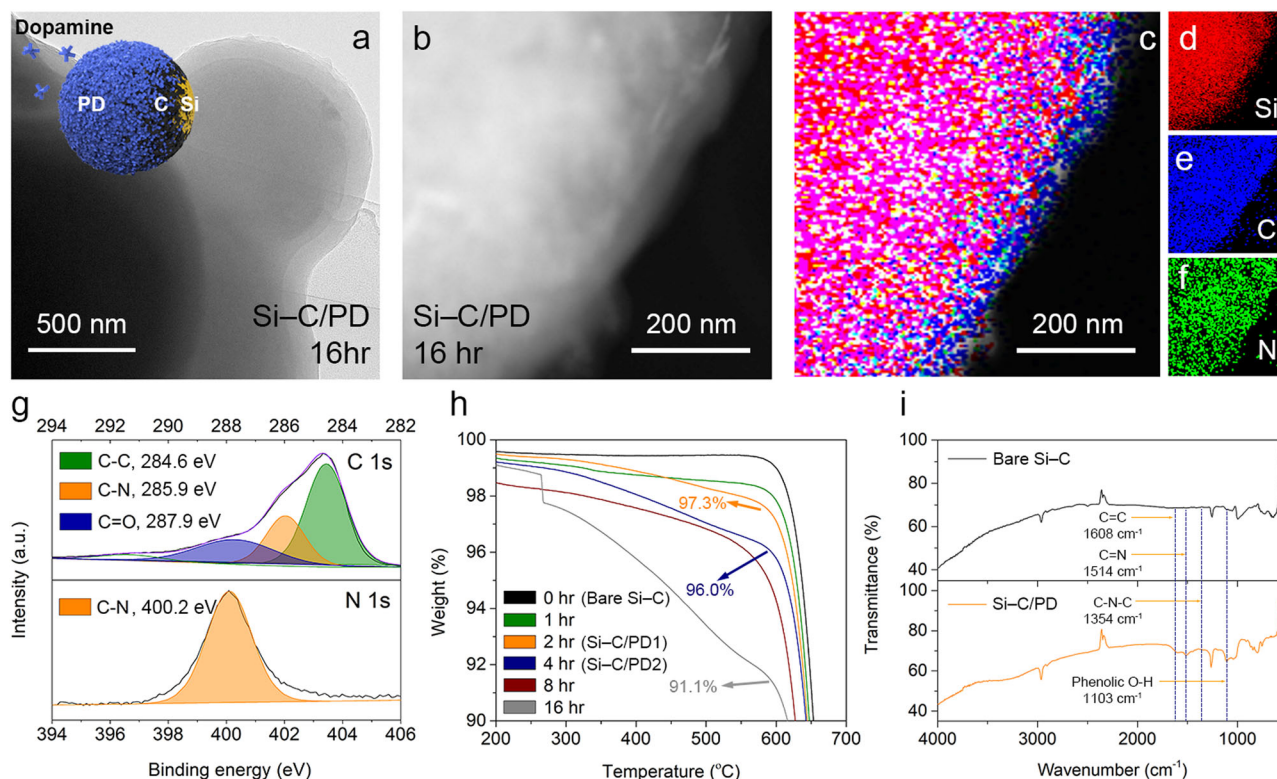
Fig. 2 | Material characterizations with and without the blocking layers. a TEM and **b** high-angle annular dark-field images of the Si–C/PD-16 h sample. **c** Overlayed EDS map of (**b**) with the signals for **d** Si, **e** C, and **f** N. **g** XPS spectra of the Si–C/PD-16 h sample with the C 1s and N 1s core–level regions. C–C, C–N, and C=O bonds are indexed as green, orange, and blue, respectively. **h** TGA curves of the samples produced after 0 h (black line), 1 h (green line), 2 h (orange line), 4 h (blue line), 8 h (brown line), and 16 h (gray line) of PD coating. **i** FT-IR spectra of the bare Si–C (black line) and Si–C/PD–16 h composites (orange line).

through electrochemical impedance spectroscopy (EIS, Supplementary Fig. 6). Notably, the electrochemical impedance decreased when the coating time was limited to 4 h, while impedance exhibited a sharp increase beyond this duration. This phenomenon can be attributed to the flocculation of Li ions within the PD layer on the Si-C composite surface, thereby enhancing ionic mobility and activity to surface reactions (Supplementary Fig. 7). Consequently, samples subjected to 2 and 4 h of coating time were designated as Si-C/PD1 and Si-C/PD2, respectively. X-ray photoelectron spectroscopy (XPS) analysis of the samples (Fig. 2g and Supplementary Fig. 8) unveiled a distinctive signal at 400.2 eV in the N 1 s core-level region of the PD-coated composites, confirming the formation of amide bonds within the PD layer on the Si-C composite surface. Thermogravimetric analysis (TGA) was employed to quantitatively assess the extent of PD coating on the Si-C composite (Fig. 2h). The Si-C composite coated with PD, generated after 16 h of oxidative polymerization, exhibited a weight loss of up to 9 wt%, whereas Si-C/PD1 and Si-C/PD2 samples contained 2.7 and 4.0 wt% of PD layers (as summarized in Supplementary Table 1). Furthermore, the chemical structure of the PD blocking layer was investigated using Fourier transform infrared (FT-IR) spectroscopy (Fig. 2i and Supplementary Fig. 9). The observed peaks at 1354, 1608, and 1514 cm^{-1} can be attributed to distinct features of PD, specifically the C-N-C bonds within the indole rings, C = C bonds, and cyclized C = N bonds of PD, respectively. These results provide conclusive evidence of the successful application of the PD layer onto the carbonaceous surface of the Si-C composite.

Cell performance tests using the ELET method and the interpretation of resulting standard contour plots

PD moieties have been effectively applied as a passivation layer on the surface of Si-C composites, anticipated to aid in the desolvation process of solvent molecules accompanying Li ions. To assess the impact of PD layers on electrolyte decomposition, particularly under lab-scale conditions with

an abundant supply of electrolyte, standard half-cell tests were carried out on Si–C/PD, utilizing ample amounts of electrolyte. Following 2 h of PD coating (Si-C/PD1), cyclic voltammetry (CV) analysis revealed distinct cathodic/anodic peaks associated with the lithiation modes of Si and C (Supplementary Fig. 10). Subsequently, cycle performance tests were conducted on bare and PD-coated composites produced after varying coating durations (Supplementary Fig. 11 and Supplementary Table 2). The sample generated after 4 h of PD coating (Si-C/PD2) exhibited a slightly enhanced cycling stability when compared to other samples with thicker PD layer coatings. The voltage profile of the Si-C/PD2 sample indicated minimal increases in overpotentials after cycling (Supplementary Fig. 12). Nevertheless, it remains uncertain whether the actual cycling stability of the Si-C, Si-C/PD1, and Si-C/PD2 samples can effectively distinguish the performance of each cell in half-cell tests. In assessments of cell performance with excessive electrolytes, quantifying the loss of active Li ions poses challenges because capacity degradation results from a combination of material electrical resistance deterioration and Li ion loss due to SEI formation. Additionally, the introduction of extra Li ions from surplus electrolytes complicates the comparison of Coulombic efficiency and capacity retention of cells, alongside those provided by the cathode. Therefore, for precise cell performance evaluation and standardization, it is imperative to accurately assess the consumption of active Li ions provided by the cathode via electrolyte decomposition while minimizing the influence of external Li sources. This is achieved through the implementation of the ELET condition.

Before proceeding with the ELET evaluation, normal full-cell tests were performed using the same electrode configurations, yet with a surplus of electrolyte (Fig. 3a, 3b). The initial capacities of the tested cells were found to be 6.44, 6.42, and 6.43 mAh for the bare Si-C, Si-C/PD1, and Si-C/PD2, respectively, with the corresponding initial Coulombic efficiencies calculated at 83.8%, 83.9%, and 84.8%. It was observed that the electrolyte decomposition tendency slightly diminished with an increase in the
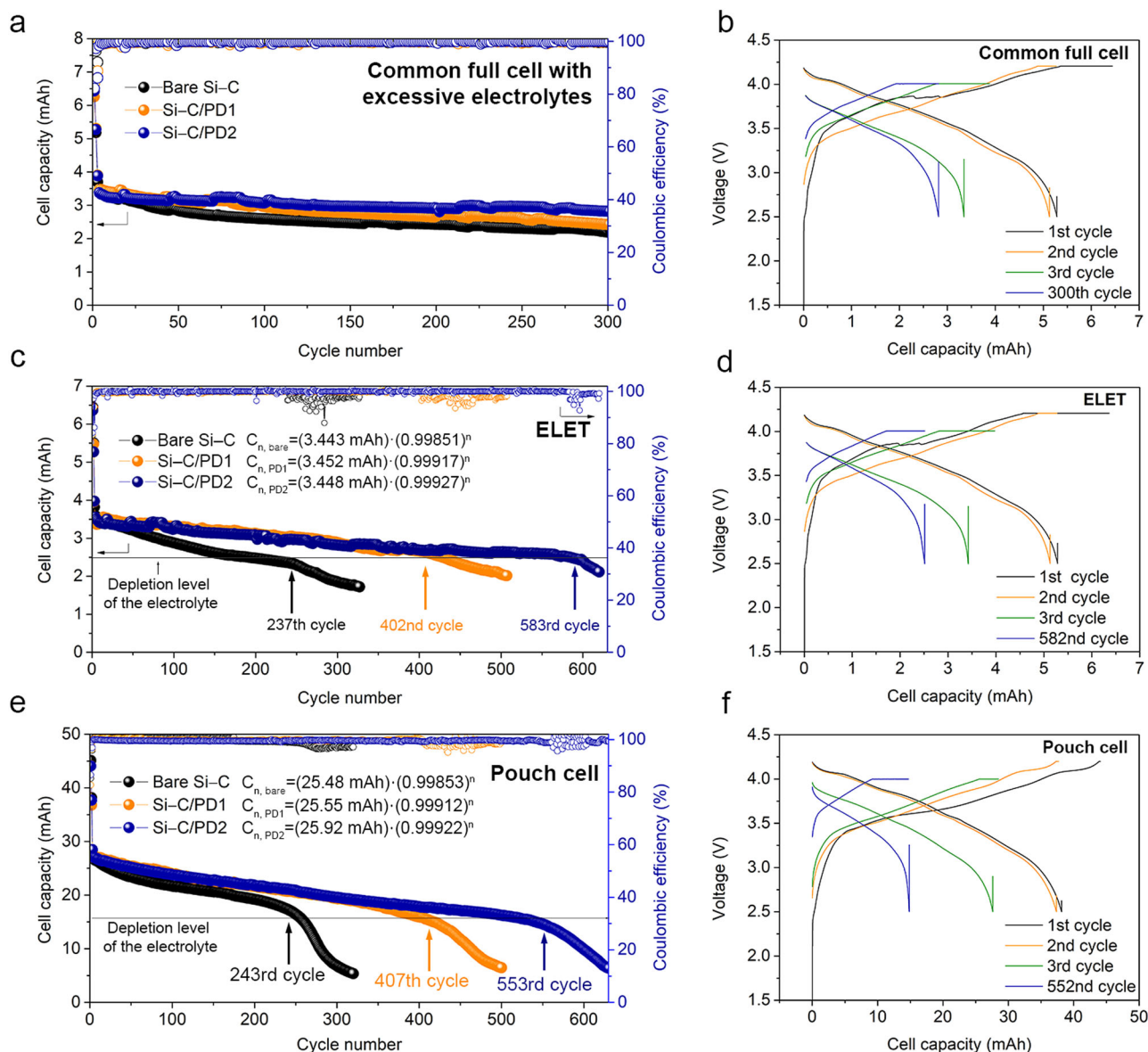
Fig. 3 | Assessing the effectiveness of the ELET method in quantifying electrolyte consumption differences between bare and PD-coated Si–C composites. a Cycle performance of the bare Si–C, Si–C/PD1, and Si–C/PD2 composites through conventional coin full cell tests. **b** Voltage profiles of the Si–C/PD2 sample obtained through the coin full cell test. **c** Cycle performance and capacitive plunging points of the bare Si–C, Si–C/PD1, and Si–C/PD2 composites. **d** Voltage profiles of the Si–C/PD2 sample determined through the ELET technique using a lean electrolyte (1.875 µl mAh^{-1}). **e** Cycle performance and capacitive plunging points of the bare Si–C, Si–C/PD1, and Si–C/PD2 composites. **f** Voltage profiles of the Si–C/PD2 sample determined using pouch cells with a lean electrolyte (1.875 µl mAh^{-1}). For the cycle performance data, black, orange, and blue circles are designated to the bare Si–C, Si–C/PD1, and Si–C/PD2 samples. For voltage profiles, black, orange, green, and blue lines correspond to the 1st, 2nd, 3rd, and plunging (last) cycles.

thickness of the PD layer, attributed to the effect of PD layer in facilitating desolvation of the electrolytic species. Upon reaching 300 cycles, the capacity retentions for the bare Si-C, Si-C/PD1, and Si-C/PD2 were 59.3%, 62.0%, and 72.5%, respectively, corresponding to capacity retention enhancements of 2.7% and 13.2% for Si-C/PD1 and Si-C/PD2 in comparison to the bare Si-C. However, these results do not conclusively demonstrate a significant difference in capacity retention between the Si–C/PD samples and the bare Si–C, leading to an ambiguous assessment of the cycle life improvement. Moreover, the excessive employment of electrolytes in the test obscured the detection of capacity plunging point over the cycles, challenging an accurate, clear, and quantitative evaluation of the cycle life of cells. However, the introduction of the ELET condition to cells offers the opportunity to systematically investigate the relationship between Li ion loss and electrolyte depletion, facilitating the establishment of a standardized mathematical framework for evaluating cell cycle life. In the

implementation of the ELET technique, coin cells were assembled using an exceedingly limited amount of electrolyte, which could be readily depleted.

These cells were subsequently subjected to mathematical modeling for comprehensive analysis (Supplementary Figs. 13–16 and Supplementary Table 3). Notably, the differences in stability curve slopes and reversible capacity (C_{rev}) values obtained through the ELET method were more pronounced (Fig. 3c and Supplementary Note 2). Moreover, the occurrence of capacitive plunging points resulting from electrolyte depletion was conspicuously evident following ELET testing. Specifically, the plunging points for each sample were observed at the 237th cycle (bare Si-C), 402nd cycle (Si-C/PD1), and 583rd cycle (Si-C/PD2). It is noteworthy that the PD-based blocking layers coated on the Si-C composite contributed to at least a 40% reduction in electrolyte decomposition. Notably, the bare Si-C sample tested with the ELET showed a lower capacity retention (64.2%) compared to the normal full cell test (65.8%). This indicates that an extremely lean electrolyte

environment is susceptible to electrolyte decomposition due to reduced interfacial contact between the electrolyte and electrode materials, where the electrolyte barely suffices to fill the pores within electrode. In contrast, during normal full cell tests with excessive electrolyte, there is no risk of electrode pores drying out due to electrolyte depletion. This condition inadvertently introduces additional electrolyte sources into the cell operation, accordingly leading to an overestimated cycle life.

Furthermore, during the voltage relaxation region between the 3rd and 582nd charging cycles, where trapped Li ions are evenly redistributed, no substantial overpotential variations were observed (Fig. 3d and Supplementary Fig. 17). Considering the marginal increase in the voltage at the end of the discharging profile, the relaxation step following galvanostatic discharge likely facilitated the uniform distribution of trapped Li ions throughout the cell system, allowing for full retrieval of Li ions[45,46]. Subsequently, with the same cell configuration, encompassing E/C and N/P (the capacity ratio of negative electrode to positive electrode) ratios, the cell performance of the prepared samples was evaluated within a pouch cell system that closely emulated the ELET conditions. Because the lean electrolyte condition depends on the characteristics of separators and electrodes, several factors attributed to the difference of cell housing systems should be considered in order to emulate the cell performance from other housing systems. This pouch cell system yielded significantly greater capacity compared to coin cells (Figs. 3e and 3f). As a result, despite disparities in cell capacity, the plunging cycle and the slope of capacity fading exhibited notable similarity, implying that cell performance under the ELET condition can effectively mirror that of large-scale cell systems, thereby facilitating standardized performance evaluation.

The ELET methodology is particularly adept at maximizing the insertion and retrieval of Li ions from the electrolyte during charge and discharge cycles. This capability allows for the formulation of a mathematical expression that captures the trend of cycle performance of battery cells based on the assumption that Li ions irreversibly consumed during cycling are exclusively utilized to generate the byproducts resulting from electrolyte decomposition. The capacity of a cell at a given cycle (C_n) during ELET testing can be mathematically expressed as a function of the reversible capacity (C_{rev}), cell electrolytic efficiency (ε), and the cycle number (n), as shown in Eq. (1) (as further detailed in Supplementary Note 2).

$$C_n = C_{rev} \cdot \varepsilon^n \tag{1}$$

Especially, ε is the term derived kinetically from the rate constant for the electrolyte decomposition, time, and growth level of the SEI layer. It signifies the electrolytic efficiency within the context of the ELET condition (Supplementary Note 2). When all of the electrodes are constructed with sufficient charge/discharge efficiency, the capacity fading primarily arises from the electrolyte decomposition, which is accompanied by an equivalent level of Li ion consumption. Accordingly, ε can effectively capture the reaction kinetics related to the formation of SEI layers (or electrolyte decomposition) with associated variables, including the rate constant for the electrolyte decomposition, time, and growth level of the SEI layer, thereby serving as an indicator of electrolytic efficiency.

Furthermore, gradual degradation of active materials, attributable to the interfacial delamination of these materials (e.g. due to the volumetric expansion of Si), adhesion failure, and structural changes, is a crucial factor in capacity fading and electrical isolation over cycles of cells. This degradation occurs progressively throughout repeated cell operation, imposing limitations on the retaining of Coulombic efficiency during cycles[47,48]. Consequently, this leads to a consistent trend in both capacity fading and a decrease in Coulombic efficiency, rather than abrupt changes in performance. However, it is essential to distinguish this from the abrupt capacitive degradation mode of capacity plunging, which deviates from the ongoing capacity trend. Therefore, a sudden drop in Coulombic efficiencies is more appropriately attributed to emergent issues during cell operation, such as the depletion of electrolytes. Basically, our ELET

approach accounts for three primary aspects: capacity, Coulombic efficiency (converted into electrolyte efficiency), and the plunging occurrence in cycle performance. The factors influencing capacity trends are consequently mirrored in the observed capacity and Coulombic efficiency of the cells. For instance, if a specific fraction of electrode materials is steadily depleted over cycles, this is manifested as decreases in both capacity and Coulombic efficiency. Since ELET performance assessments are based on actual cell operation results, it can be inferred that the ELET evaluation inherently considers various factors impacting the capacity trend of cells.

To evaluate cell performance before reaching the capacitive plunging point, it is possible to calculate the total cell capacity required to decompose 1 μl of the electrolyte (c_{total} with a unit of mAh μl^{-1}) using Eq. (2) (as further explained in Supplementary Note 3)

$$c_{total} = \frac{C_{rev}}{V_{electrolyte}} \left(\frac{1 - \varepsilon^{n_p+1}}{1 - \varepsilon} \right), \left(\sum_{n=1}^{3} C_{n,\exp} \ll C_{total} \right) \tag{2}$$

where $V_{electrolyte}$ represents the volume of the electrolyte introduced into the cell for ELET, n_p is the plunging cycle and $C_{n,\exp}$ denotes the experimental cell capacity at a specific cycle. As a result, when c_{total} is represented as a 3D contour plot using Eq. (2), it generates an evaluation map displaying c_{total} values (Fig. 4a).

For instance, plotting c_{total} as a function of $V_{electrolyte}$ and ε enables the capacity trends of the cells to align with those of commercial cell systems based on the quantity of electrolyte employed. Furthermore, ε functions as a unique characteristic of active materials, determined by the extent of electrolyte decomposition reactions induced by these materials. This characteristic facilitates standardized performance comparisons across various material types and battery systems. By selecting suitable values for C_{rev} and $V_{electrolyte}$ within the ELET technique, a two-dimensional (2D) contour map of c_{total}, as a function of electrolytic efficiency and plunging cycle, can be constructed using Eq. (2) (Fig. 4b and Supplementary Fig. 18). The electrolytic efficiency of the bare Si-C composite was determined to be 0.99851, with its capacitive plunging point occurring after the 237th cycle. Based on these values, the c_{total} of the bare composite was determined to be 57.6 mAh μl^{-1}. Conversely, following the implementation of PD layer coatings, the electrolytic efficiencies for the Si–C/PD1 and Si–C/PD2 samples increased to 0.99917 and 0.99927, respectively. Correspondingly, the plunging points were significantly extended to the 402nd and 583rd cycles for these samples, respectively. As a result, the c_{total} values of the Si–C/PD1 and Si–C/PD2 samples markedly increased to 98.6 and 138.6 mAh μl^{-1}, respectively. This proves the significance of employing electrolyte-blocking layer coatings on active materials as an effective means to mitigate electrolyte decomposition.

The ELET method was primarily developed based on the electrolyte depletion behavior observed during cell cycling, which is a phenomenon that similarly affects most post-secondary batteries, which means the ELET method has a potential to be universally applied to other battery systems. Moreover, the extent of this effect varies depending on the type of specific core materials used in electrodes, current collectors, and electrolytes. To validate its versatility across various cell configurations, the ELET technique was extended to two types of Li metal battery systems composed of a combination of Li anode/S cathode and Li anode/ LiNi$_x$Co$_y$Al$_z$O$_2$ (NCA) cathode (Supplementary Figs. 19 and 20). The electrolytic efficiency for the Li–S and Li-NCA cell systems was calculated to be 0.99602 and 0.99418, and the plunging points occurred after the 44th and 24th cycle, respectively. In case of Li-NCA system, the voltage window and operating voltage is immensely higher than that of Li-S batteries, leading to the lower electrolytic efficiency. Using these values, the calculated c_{total} values for the Li-S and Li-NCA system were determined to be 11.6 mAh μl^{-1} and 11.7 mAh μl^{-1}. Despite its relatively lower electrolytic efficiency, the Li-NCA system exhibited a similar c_{total} value due to the higher specific reversible capacity of 5.62 mAh μl^{-1}, surpassing that of the Li-S system.
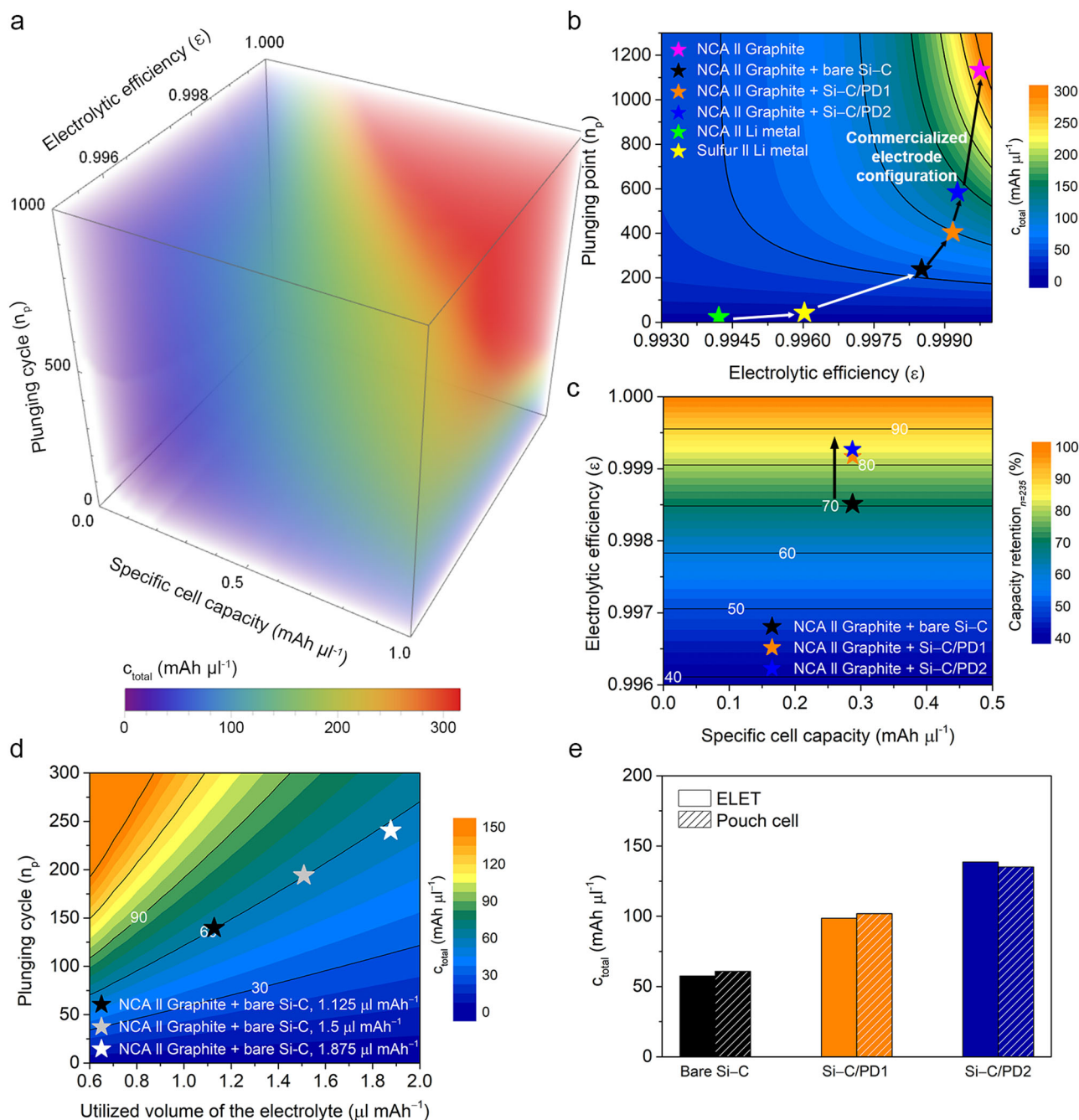
Fig. 4 | Contour plots constructed using ELET-based calculations for assessing cell cycle performance. a 3D contour map illustrating cell performance as a function of specific capacity, plunging cycle (n), and electrolytic efficiency (ε). **b** 2D contour plot of c_{total} considering ε and n_p. Pink, blue, orange, black, yellow, and green stars are designated to NCA–graphite, NCA–graphite/Si–C/PD2, NCA–graphite/Si–C/PD1, NCA–graphite/bare Si–C, sulfur–Li, and NCA–Li cells. **c** 2D contour plot depicting capacity retention at 235th cycle in relation to the specific cell capacity (C_{rev}) and ε, where black, orange, and blue stars are designated NCA–graphite/bare Si–C, NCA–graphite/Si–C/PD1, and NCA–graphite/Si–C/PD2 cells. **d** ELET results with varying electrolyte contents, where black, gray, and white stars are designated to the cells with E/C ratios of 1.25, 1.5, and 1.875 μl mAh⁻¹, respectively. **e** Comparison of c_{total} values obtained from ELET and pouch cell tests. Bare Si-C, Si–C/PD1, and Si–C/PD2 samples are indexed as black, orange, and blue colors, respectively. c_{total} values obtained from ELET and pouch cell performance are indexed as plain and dashed patterns, respectively.

In contrast, when evaluating a commercialized cell configuration involving a graphite anode and a Ni-Co-Al oxide (NCA) cathode, the c_{total} was found to be 286.1 mAh μl⁻¹, with an electrolytic efficiency of 0.99975 and a plunging cycle after the 1136th cycle. Notably, the overall performance of the LSB system was ~25 times lower than that of the commercialized LIB system (Fig. 4b and Supplementary Fig. 21). The results obtained through the ELET technique were concisely summarized in both tabular and graphical formats (Supplementary Fig. 22

and Supplementary Table 4). Despite the LSB system boasting a higher specific capacity compared to the LIB system, its comparatively inferior cyclic stability presents a significant challenge to its commercial viability. As a result, c_{total} emerges as a standardizable metric for assessing the performance of diverse battery operating systems, even when composed of distinct components.

Alternatively, capacity retention can be assessed using Eq. (3), taking into account the electrolytic efficiency determined through the ELET

technique (as further detailed in Supplementary Note 4),

$$Capacity\ retention\ (\%) = \frac{C_n}{C_0} \times 100\% = \varepsilon^n \times 100\% \qquad (3)$$

where C_0 is the capacity at the 1st cycle. The capacity retention, which is a common indicator for the cycle life of batteries, could be derived using the ε and cycle number, as described in Eq. (3). By applying Eq. (3), a 2D contour map of capacity retention at a specific cycle can be constructed, considering the specific cell capacity and ε (Fig. 4c). After the 235th cycle, for example, the capacity retention of the bare Si-C composite was determined to be 70.4%. In contrast, the Si-C/PD1 and Si-C/PD2 samples exhibited capacity retentions of 85.2% and 87.9% at the same cycle, respectively. Therefore, ε serves as a suitable conversion factor for capacity retention, which is commonly employed to assess cell performance.

Furthermore, both experimental and mathematical validation confirmed that c_{total} values obtained from the same material remain consistent regardless of the electrolyte volume utilized during cell operation, while a reduction in electrolyte volume expedites the onset of the plunging cycle (Fig. 4d, Supplementary Fig. 23, and Supplementary Note 5). In detail, when utilizing 60% and 80% of the electrolyte relative to 1.875 µl mAh⁻¹, the plunging cycles were respectively shortened by 59.5% and 82.3%. However, since c_{total} is a value based on a unit volume of electrolyte, it can be maintained without significant change regardless of the quantity of electrolyte consumed. In practice, it has been observed that c_{total} values in cases where 60% and 80% of the electrolyte was used relative to 1.875 µl mAh⁻¹ were 60.9 mAh µl⁻¹ and 60.8 mAh µl⁻¹, respectively. This suggests that c_{total} could serve as a unique indicator for assessing cell performance because it remains unaffected by variations in the volume of electrolyte. These c_{total} values exhibit remarkable consistency and can be consistently reproduced regardless of both the amount of electrolyte and the type of cell system. When c_{total} values were derived from cycle data obtained from pouch cells, they were nearly identical, showing no significant discrepancies among the samples (Fig. 4e). Indeed, coin and pouch cells exhibit different operational characteristics, despite employing identical electrodes and electrolytes. Three key differences are particularly noted: the electrolyte-wetting behavior within electrodes influenced by applied cell pressure, the cell resistance stemming from tap-welding, and the used surface area of separators. Among these, the reduced cell resistance in pouch cells, assuming sufficient electrolyte-wetting in both cell types, is a critical factor distinguishing them from coin cells. This difference in resistance, typically lower in pouch cells even when fabricated with electrode-housing welding processes, contributes to gaps in obtained capacity performance between the two cell types.

To mitigate this difference, a potentiostatic charging step follows galvanostatic charging, aiming to maximize the lithiation process. However, an extended potentiostatic charging phase holds the cell in a high voltage region for a longer period, potentially accelerating electrolyte decomposition and Li⁺ consumption compared to pouch cells[49]. Consequently, the analyzed c_{rev} values (C_{rev} term in ELET divided by the total volume of electrolytes) are higher in pouch cells than in those evaluated by the ELET method. Moreover, the loss of active Li ions in coin cells during the first cycle could result in relieved volumetric expansion of Si, thereby enhancing the electrolytic efficiency of coin cells. Despite this, the similarity in c_{total} values for both cell types can be attributed to the balancing effect of lower c_{rev} values offsetting the increased electrolytic efficiency in coin cells, which enables consistent performance evaluation across different cell types. This implies that c_{total} has the potential to predict the cell performance of materials in large-scale cells, even when tested in small-scale cell configurations, thereby allowing for the implementation of standardized performance evaluation of battery cells.

Meanwhile, it is noteworthy that the ELET method has the capability to evolve into a performance metric based on energy density, rather than just capacity. This shift in focus is significant because the fabrication structure of cells influences their volume and weight. For instance, while cylindrical and pouch cells differ in stacking format and structure, their electrochemical reactions are fundamentally identical and fully reliant on the cell

components. Provided the cells are assembled using uniform fabrication processes, including tapping, welding, and degassing, and are free from extraneous factors, they should exhibit mostly similar performance. However, due to the wound structure of the electrode, cylindrical cells are more susceptible to external forces, which may lead to unexpected variations in performance, particularly when implemented in real-world devices. Cylindrical cells incorporate a core cylinder (axis) to facilitate electrode rolling, a feature not required in pouch cells. Such disparities in housing components can impact the overall weight and volume of the cells. Therefore, it may be necessary to incorporate an additional correcting factor in the ELET method to account for these differences.

Integrated analyses on the growth of the SEI layers

To ensure the reliability and consistency of the proposed ELET technique, the cells underwent post-cycling characterization to quantitatively assess the growth of SEI layers formed as a result of electrolyte decomposition. To induce sufficient electrolyte decomposition, the cells were cycled at a rate of 0.5 C using the conventional half-cell configuration with an excess of electrolyte (Fig. 5a). Upon analyzing the trend of SEI formation by comparing the anodic sweeps of the first cycle among the prepared samples, it was observed that the intensity of the anodic peaks in the voltage range of 0.5–1.0 V, which is associated with SEI formation, decreased after the application of PD layers (Fig. 5b). This reduction in peak intensity indicates that PD layers have the capacity to alleviate the level of electrolyte decomposition.

Furthermore, the progression of SEI film growth over cycling was tracked by assessing changes in cell impedance through EIS analyses (Figs. 5c–5e and Supplementary Table 5). To examine the evolution of the SEI film during cycling, impedance measurements obtained after the 1st and 100th cycles were compared. Specifically, the first semicircle in the Nyquist plots was considered, as it is related to the resistance of the active material surface. The initial impedance of the first semicircle for the bare Si–C composite doubled after 100 cycles. This increase suggests that after 100 cycles of cell operation, the surface of the bare sample was extensively covered with SEI layers, potentially impeding the electrical conduction of the active materials. In contrast, the impedances of the Si–C/PD1 and Si–C/PD2 samples only experienced a slight increase even after 100 cycles of cell operation, indicating the minimal growth of the SEI layer due to the suppression of the electrolyte decomposition by the PD-based blocking layer. In turn, the inhibition of SEI layer growth likely contributed to the improved electrolytic efficiencies of the Si–C/PD samples, ultimately delaying their capacitive plunging cycles.

To quantify the growth of the SEI layer, direct XPS and XRD measurements were conducted using the spent electrodes after 100 cycles of operation. These analyses allowed for an examination of the internal chemical and crystallographic compositions of the disintegrated cells. In the XPS spectra of all the samples, peaks at 55.4 and 56.3 eV were observed, which can be attributed to Li_2CO_3 and LiF, respectively (Fig. 5f). These Li-based compounds are the primary constituents of the SEI layers. However, the peak corresponding to LiF in the XPS spectrum of the Si–C/PD2 sample was less prominent and weaker compared to the spectra of the bare Si–C and Si–C/PD1 composites. This observation suggests a reduction in the decomposition of fluoroethylene carbonate within the electrolyte and, consequently, the suppressed formation of LiF in the Si–C/PD2 sample (Supplementary Fig. 24).

In addition, the amounts of the Li_2CO_3 and LiF phases were determined through XRD analysis (Fig. 5g). Notably, no peak corresponding to Si was detected in the XRD patterns of all the samples, primarily due to the prevalent amorphization of Si during cell cycling. The peak at $2\theta = 26.5°$ can be attributed to the carbon-based materials present in the electrodes, which include soft carbon and conductive additives. On the other hand, the peak at $2\theta = 37.5°$ can be assigned to the Al-based sample holder used in the XRD measurements (Supplementary Fig. 25). Additional peaks that can be attributed to the formation of the SEI films in the electrodes after the cycling were observed, which were absent in the patterns of the unused electrodes
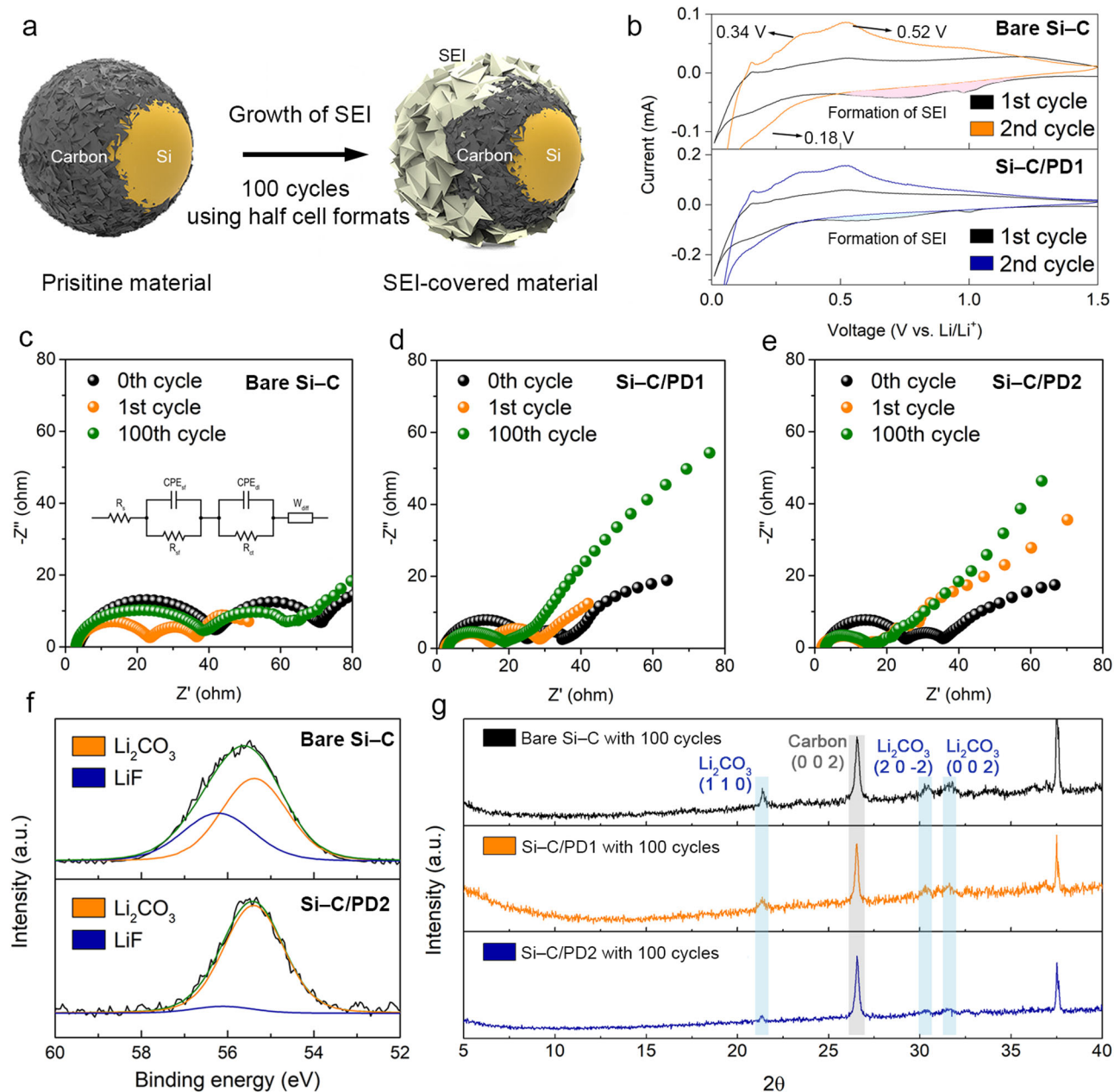
Fig. 5 | Analyses of the cells after 100 cycles of cell operation. a Schematic depicting the formation of the SEI layer after cycling. **b** Cyclic voltammetry curves of the bare Si–C and Si–C/PD1 samples after the 1st (black line) and 2nd cycles (orange and blue lines for the bare Si–C and Si–C/PD1, respectively). Nyquist plots of the **c** bare Si–C, **d** Si–C/PD1, and **e** Si–C/PD2 samples after 0 (black circles), 1 (orange circles), and 100 cycles (green circles). **f** Li 1s core–level region of the XPS spectra of the bare Si–C and Si–C/PD2 electrodes after 100 cycles of cell operation, where blue and orange lines are assigned to LiF and Li_2CO_3, respectively. **g** XRD patterns of the bare Si–C (black line), Si–C/PD1 (orange line), and Si–C/PD2 sample (blue line) after 100 cycles of cell operation.

(Supplementary Fig. 26). Specifically, the peaks at $2\theta = 21.4°$, 30.3°, and 31.6° corresponded to the (110), ($20\bar{2}$), and (002) planes of the crystalline Li_2CO_3 phase, respectively. The peaks indicative of the Li_2CO_3 phase in the XRD pattern of the bare Si–C composite were sharper and more intense compared to those in the patterns of the PD-coated samples. This indicates that more Li_2CO_3 was generated on the bare sample after cycling, possibly due to the poorly controlled growth of the SEI layer. Therefore, the XPS and XRD results align with the EIS measurements, revealing that the introduction of the PD blocking layer effectively suppressed the electrolyte decomposition.

Furthermore, majority of the O and F signals observed in the EDS elemental maps of cross-sectional images, which indicates the presence of SEI layers, were significantly reduced in PD coated samples (Supplementary Fig. 27). Additionally, the d-spacings of the crystallites obtained through

selected area diffraction correlates well with those of the (201) and ($40\bar{2}$) planes of Li_2CO_3 (Supplementary Fig. 28). Therefore, the region with strong O and F signals was identified as the grown SEI phase. Overall, the proposed components and variables for the ELET technique can successfully describe the extent of electrolytic decomposition, as confirmed by the results of the crystallographic, chemical, and imaging analyses.

Conclusions

In this study, a standardized cell testing technique was introduced, providing an evaluation method for cell performance under ELET conditions. The ELET technique enabled the determination of reversible capacity, electrolytic efficiency, and plunging points of cells, which are essential metrics for rate capability, electrolyte decomposition levels, and cell cycle

life. These properties were shown to be compatible with those of commercial pouch cells. One of the notable features of the ELET technique is the use of a quantitatively fixed lean amount of electrolyte, which allows for the establishment of mathematical relationships and accurate evaluation of cell performance across different battery systems and cell components, reflecting the cell performance under the practical scale of applications. When the ELET performance was compared with that of the pouch cell, we confirmed the compatibility of ELET performances with the practical scale of pouch cell performances. The study also demonstrated the effectiveness of a PD-based coating in suppressing electrolyte decomposition on Si–C composite-based anodes using the proposed ELET method. The PD coating acted as an electrolyte-blocking layer, preventing solvent molecules from reaching the electrochemically active surfaces of the materials and improving electrolyte preservation. The ELET measurements revealed that the PD-coated sample significantly extended its plunging point, indicating a 150% reduction in electrolytic decomposition compared to the bare Si–C composite. Notably, the PD layers induces 13%-improved cyclic stability after 300 cycles of cell operations through the normal full-cell test, which proves the superior feature of the ELET measurement as a highly discernable evaluation platform for cell cycle life. Overall, the introduced ELET technique holds promise for advancing the development of next-generation battery systems and conventional high-capacity LIBs. It provides a rational and standardized approach to evaluating the performance of high-performance materials across various battery systems, which can contribute to advancements in practical battery applications.

Methods
Materials
Si nanoparticles (~80 nm, CN Vision), coal-tar pitch (Samsung SDI), dopamine hydrochloride (≥98.0%, Sigma-Aldrich), hexylamine (≥99.0%, Sigma-Aldrich), poly(acrylic acid) (M_w = 250,000, 35 wt% in H_2O, Sigma-Aldrich), carboxymethyl cellulose (M_w = 700,000, Sigma-Aldrich), and styrene–butadiene rubber (SBR, MTI Korea), ethanol (≥ 99.5%, Sigma-Aldrich), 1.3 M $LiPF_6$ in a 3:7 (v/v) mixture of ethylene carbonate and dimethyl carbonate (DMC) with 5 wt% fluoroethylene carbonate (Dongwha Electrolyte), 1.0 M LiTFSI in a 5:5 (v/v) mixture of dimethoxyethane (DME) and dioxolane (DOL) with 2 wt% $LiNO_3$ (Dongwha Electrolyte), Super P (Wellcos Corporation).

Synthesis of the bare Si–C composites
To synthesize the bare Si–C complexes, Si nanoparticles (1 g) were mechanically ball-milled with coal-tar pitch (2 g) for 20 min using zirconia balls. Then, the Si–pitch mixture was annealed at 900 °C for 2 h at a ramp rate of 3 °C min^{-1} under an Argon environment to carbonize the blended pitch. After cooling down the carbonized samples, they were mechanically ball-milled for another 10 min to finely ground the particles. Finally, the sample was carefully refined using a molecular sieve with a pore size of 635 mesh. The collected sample was labeled as the bare Si–C composite.

Synthesis of the Si–C/PD composites
The Si–C/PD samples were synthesized through a solution-based PD coating procedure using the as-prepared bare Si–C composite. First, the bare Si–C composite (0.5 g) was dispersed in ethanol (final concentration = 10 mg ml^{-1}) through tip-induced ultrasonication for 30 min. To adjust the pH to alkaline conditions, hexylamine (200 ml) was added to the bare Si–C dispersion after the sonication, followed by mild stirring for 5 min. Then, the dopamine monomer (0.5 g) was added, and the resulting solution was continuously agitated for the specified coating duration (1, 2, 4, 8, and 16 h). After the agitation, the solution was rinsed for five times with ethanol and ultra-centrifugated using 50 ml conical tubes. The solid samples that settled in the conical tubes were dried at 70 °C for 3 h under vacuum. Finally, the samples were ground using a mortar and pestle and filtered through a molecular sieve with a pore size of 635 mesh.

Material characterizations
Fourier-transform infrared (FT-IR) spectroscopy (IFS-66/S, Bruker Corporation) was performed to study the molecular structure of the PD coating. To determine the actual amount of the carbon and PD layers in composites, thermogravimetric analysis (TGA) (TG/DTA7300, SEICO Inst.) was conducted up to 900 °C in air at a heating rate of 10 °C min^{-1}. Powder X-ray diffraction (XRD, D8 Focus, Bruker AXS) measurements were recorded from 2θ = 5° to 80° at a step size of 0.02° s^{-1} using a Cu K$_\alpha$ radiation (λ = 1.5406 Å). The thicknesses of the PD layers, surface morphologies, and chemical compositions of the samples were examined through high-resolution transmission electron microscopy (HR-TEM, JEM-ARM-200F, JEOL); the corresponding energy dispersive X-ray spectroscopy (EDS) was employed for elemental analysis. After the cell cycling, X-ray photoelectron spectroscopy (XPS, ESCALAB250, Thermo Fisher) was performed using powder samples of electrodes extracted from the used cells.

Electrode preparation and battery tests using conventional half-cell setup
To prepare the working electrodes, each sample was mixed with conductive carbon black (Super P) and poly(acrylic acid) in ethanol at a mass ratio of 70:15:15 in a mortar and pestle to form a homogeneous slurry. The resulting slurry was then uniformly coated on a Cu foil using a doctor blade and then dried at 110 °C for 5 min. Prior to cell assembly, the electrode was dried at 120 °C for 3 h under vacuum. The electrode loading was 2.3 mg cm^{-2}, and the resulting film density was 0.6 g cm^{-3}. The coin cells were assembled for the conventional half-cell tests using the as-prepared electrodes with a diameter of 8 pi. Li metal and polyethylene (the thickness of 16 μm, Hipore, Asahi Kasei) were used as the counter electrode and separator, respectively. A $LiPF_6$ solution (1.3 M) in a 3:7(v/v) mixture of ethylene carbonate and dimethyl carbonate (DMC) with 5 wt% fluoroethylene carbonate was used as the electrolyte for the LIB system. For the LSB system, a LiTFSI (1.0 M) solution in a 1:1(v/v) mixture of dimethoxyethane (DME) and dioxolane (DOL) with 2 wt% $LiNO_3$ was used as the electrolyte. The cells were assembled in a glovebox at a relative humidity of ≤ 1 ppm.

A multichannel potentiostat/galvanostat (WMPG 1000, WonATech) was used for the cycling tests. At the first cycle, galvanostatic discharge at 0.1 C was performed to 0.01 V in a constant current mode. Then, potentiostatic discharge at 0.01 V was performed up to 0.01 C of the cut-off current at a constant voltage mode to maximize the lithiation of the working electrode. This was followed by a galvanostatic charge to 1.5 V with 0.1 C. From the second cycle, galvanostatic discharge to 0.01 V with 0.5 C in a constant current mode and potentiostatic discharge at 0.01 V up to 0.05 C were performed. These were followed by a galvanostatic charging step to 1.5 V with 0.5 C. This process was repeated for 100 cycles. For the measurement of the rate performance, the C-rate was increased every 10 cycles with the same potential range between 0.01 and 1.5 V (vs Li/Li$^+$) at current densities ranging from 300 to 10000 mA g^{-1} except for the first cycle, which was performed at 100 mA g^{-1}. The specific capacities were calculated using the total amount of the active material contained in the electrodes. Cyclic voltammetry was carried out at a scan rate of 0.1 mV s^{-1} from 0.01 to 1.5 V. Electrochemical impedance spectroscopy (EIS, CHI6143E, CH Instruments, Inc.) measurements were performed at an AC oscillation amplitude of 5 mV from 100 kHz to 0.01 Hz.

Electrode preparation and battery tests through the ELET method and pouch cells
To prepare the working electrodes for the ELET technique, each sample was ball-milled with graphite to achieve a specific cell capacity of 500 mAh g^{-1}. To form the electrode, a homogenous slurry was prepared by mixing conductive carbon black (Super P), carboxymethyl cellulose (Mw = 700,000, Sigma-Aldrich), and styrene–butadiene rubber (SBR, MTI Korea) with water at a mass ratio of 96:1:1.5:1.5 using a mortar and pestle. Then, the slurry was uniformly coated on a Cu foil using a doctor blade and then dried at 110 °C. The electrode loading was precisely adjusted to 6.9 mg cm^{-2} with a film density of approximately 1.6 g cm^{-3}. This corresponded to an areal

capacity of approximately 3.3 mAh cm^{-2}. Immediately after, the electrode was dried again at 120 °C for 3 h under vacuum. The full cells were then assembled using an NCA cathode (diameter = 15 pi) with a capacity of 3 mAh cm^{-2} and the as-prepared electrode (diameter = 16 pi) for the LIB system. The capacity ratio between the cathode and anode was 1:1.2 considering the total capacity of the electrodes and not the areal capacity. This condition was also employed for the ELET of the LSB system. The electrolytes, separator, coin cell type, and cell testing machine were the same as those used in the conventional half-cell tests. However, the amount of the injected electrolyte was limited to 1.875 μl per cell capacity considering the absolute capacity of the anode.

During the first cycle, galvanostatic charging with 0.1 C was performed to 4.2 V in a constant current mode wherein the C-rate was defined as the absolute capacity of cathode. Then, a potentiostatic charge step at 4.2 V up to 0.01 C was performed in constant voltage mode to maximize the lithiation of the working electrode. This was followed by a galvanostatic discharging step to 2.5 V with 0.1 C. The cell was subjected to a resting stage for 10 min to ensure the complete retrieval of the Li ions, which leads the significant changes of diffusion of ionic species in the electrode up to first 10 min. At the second cycle, galvanostatic charging to 4.2 V was performed at 0.2 C in a constant current mode. Then, potentiostatic charging at 4.2 V was conducted up to 0.01 C. This was followed by a galvanostatic discharge step to 2.5 V at 0.2 C. The cell was rested for 10 min. From the third cycle, the cell was subjected to galvanostatic charging to 4.0 V at 1.0 C and potentiostatic charging at 4.0 V up to 0.05 C. This was followed by a galvanostatic discharge step to 2.5 V at 1.0 C and a resting time of 10 min. The charging/ discharging cycles were repeated until cell death. For the LSB system, the applied current was similar to that used for the testing of the LIB. However, the voltage range and C-rate were changed to 1.7–2.8 V and 0.5 C, respectively, after the third cycle. The electorlytic efficiecny (ε) and reversible cell capacity (C_{rev}) terms were obtained by the nonlinear regression with a function shape of y=AB^x.

For the pouch cell test, pouch cell was designed with 35 mm × 35 mm size of a cathode and 37 mm × 37 mm size of an anode. The N/P ratio was 1.2 and the cell fabrication was processeed in a dry room. The a separator was used with the size of 43 mm × 43 mm, and cell components were vacuum-sealed with an Al pouch. Finally, the amount of used liquid electrolyte was set, same with the ELET method.

Post-cycling analyses
Post-cycling analyses were performed on half of the cells that completed 100 cycles of operation. The coin cells were disassembled in a glove box, and the electrodes were carefully retrieved from the cells. The electrodes were rinsed using DMC for five times in a glove box. After rinsing, the electrodes were dried in a vacuum oven at 70 °C for 30 min and then used for the XPS, XRD, and SEM analyses. Cross-sectional images were obtained using a focused ion beam system (FIB, JIB-4601F, JEOL) with a Ga liquid metal ion source at a tip current and voltage of 60 nA and 30 kV, respectively. After lifting the cross sections from the electrodes, each sample was placed on a Cu grid for TEM observation.

Data availability
The data that support the findings of this study are available on request from the corresponding author P.J.Y.

References
1. Choi, G. H. et al. Modularly aromatic-knit graphitizable phenolic network as a tailored platform for electrochemical applications. *Energy Environ. Sci.* **14**, 3203–3215 (2020).
2. Sung, J. et al. Subnano-sized silicon anode via crystal growth inhibition mechanism and its application in a prototype battery pack. *Nat. Energy* **6**, 1164–1175 (2021).
3. Shen, Y. et al. Effective chemical prelithiation strategy for building a silicon/sulfur Li-ion battery. *ACS Energy Lett* **4**, 1717–1724 (2019).
4. Park, S. et al. High areal capacity battery electrodes enabled by segregated nanotube networks. *Nat. Energy* **4**, 560–567 (2019).
5. Ko, M. et al. Scalable synthesis of silicon-nanolayer-embedded graphite for high-energy lithium-ion batteries. *Nat. Energy* **1**, 16113 (2016).
6. Zhao, C. et al. A high-energy and long-cycling lithium–sulfur pouch cell via a macroporous catalytic cathode with double-end binding sites. *Nat. Nanotechnol.* **16**, 166–173 (2021).
7. Kang, N. et al. Cathode porosity is a missing key parameter to optimize lithium-sulfur battery energy density. *Nat. Commun.* **10**, 4597 (2019).
8. Hu, Y. et al. Strategies toward high-loading lithium–sulfur battery. *Adv. Energy Mater.* **10**, 2000082 (2020).
9. Chen, W. et al. Atomic interlamellar ion path in high sulfur content lithium-montmorillonite host enables high-rate and stable lithium–sulfur battery. *Adv. Mater.* **30**, 1804084 (2018).
10. Ng, S.-F., Lau, M. Y. L. & Ong, W. -J. Lithium–sulfur battery cathode design: tailoring metal-based nanostructures for robust polysulfide adsorption and catalytic conversion. *Adv. Mater.* **33**, 2008654 (2021).
11. Asadi, M. et al. A lithium–oxygen battery with a long cycle life in an air-like atmosphere. *Nature* **555**, 502–506 (2018).
12. Xia, C. et al. A high-energy-density lithium-oxygen battery based on a reversible four-electron conversion to lithium oxide. *Science* **361**, 777–781 (2018).
13. Shu, C. et al. Understanding the reaction chemistry during charging in aprotic lithium–oxygen batteries: existing problems and solutions. *Adv. Mater.* **31**, 1804587 (2019).
14. Ye, L. et al. Stabilizing lithium into cross-stacked nanotube sheets with an ultra-high specific capacity for lithium oxygen batteries. *Angew. Chem. Int. Ed* **58**, 2437–2442 (2019).
15. Wang, A. et al. Review on modeling of the anode solid electrolyte interphase (SEI) for lithium-ion batteries. *Npj Comput. Mater.* **4**, 1–26 (2018).
16. Yang, G. et al. Robust solid/electrolyte interphase (SEI) formation on Si anodes using glyme-based electrolytes. *ACS Energy Lett* **6**, 1684–1693 (2021).
17. Balasubramanian, M. et al. Formation of SEI on cycled lithium-ion battery cathodes: soft X-ray absorption study. *Electrochem. Solid-State Lett* **5**, A22 (2001).
18. Guan, P., Liu, L. & Lin, X. Simulation and experiment on solid electrolyte interphase (SEI) morphology evolution and lithium-ion diffusion. *J. Electrochem. Soc.* **162**, A1798–A1808 (2015).
19. Ramasubramanian, A. et al. Lithium diffusion mechanism through solid–electrolyte interphase in rechargeable lithium batteries. *J. Phys. Chem.* **123**, 10237–10245 (2019).
20. von Kolzenberg, L., Latz, A. & Horstmann, B. Chemo-mechanical model of SEI growth on silicon electrode particles. *Batter. Supercaps* **5**, e20210021 (2022).
21. Ge, M. et al. Recent advances in silicon-based electrodes: from fundamental research toward practical applications. *Adv. Mater.* **33**, 2004577 (2021).
22. Kwabi, D. G. et al. Chemical instability of dimethyl sulfoxide in lithium–air batteries. *J. Phys. Chem. Lett.* **5**, 2850–2856 (2014).
23. Yim, T. et al. Effect of chemical reactivity of polysulfide toward carbonate-based electrolyte on the electrochemical performance of Li–S batteries. *Electrochim. Acta* **107**, 454–460 (2013).
24. Qiao, Y. et al. A high-energy-density and long-life initial-anode-free lithium battery enabled by a Li$_2$O sacrificial agent. *Nat. Energy* **6**, 653–662 (2021).
25. Xu, Z., Yang, J., Li, H., Nuli, Y. & Wang, J. Electrolytes for advanced lithium ion batteries using silicon-based anodes. *J. Mater. Chem. A* **7**, 9432–9446 (2019).

26. Zhao, M. et al. Lithium–sulfur batteries under lean electrolyte conditions: challenges and opportunities. *Angew. Chem. Int. Ed* **59**, 12636–12652 (2020).

27. Chen, K., Yang, D.-Y., Huang, G. & Zhang, X.-B. Lithium–air batteries: Air-electrochemistry and anode stabilization. *Acc. Chem. Res.* **54**, 632–641 (2021).

28. Chen, S. et al. Critical parameters for evaluating coin cells and pouch cells of rechargeable Li-metal batteries. *Joule* **3**, 1094–1105 (2019).

29. Gao, Y. et al. Polymer–inorganic solid–electrolyte interphase for stable lithium metal batteries under lean electrolyte conditions. *Nat. Mater.* **18**, 384–389 (2019).

30. Nagpure, S. C. et al. Impacts of lean electrolyte on cycle life for rechargeable Li metal batteries. *J. Power Sources* **407**, 53–62 (2018).

31. Chae, S. et al. Gas phase synthesis of amorphous silicon nitride nanoparticles for high-energy LIBs. *Energy Environ. Sci.* **13**, 1212–1221 (2020).

32. Wu, H. et al. Stable cycling of double-walled silicon nanotube battery anodes through solid-electrolyte interphase control. *Nat. Nanotechnol.* **7**, 310–315 (2012).

33. Meng, N., Lian, F. & Cui, G. Macromolecular design of lithium conductive polymer as electrolyte for solid-state lithium batteries. *Small* **17**, 2005762 (2021).

34. Liu, W., Liu, P. & Mitlin, D. Review of emerging concepts in SEI analysis and artificial SEI membranes for lithium, sodium, and potassium metal battery anodes. *Adv. Energy Mater.* **10**, 2002297 (2020).

35. Nam, H. G., Nam, M. G., Yoo, P. J. & Kim, J.-H. Hydrogen bonding-based strongly adhesive coacervate hydrogels synthesized using poly (N-vinylpyrrolidone) and tannic acid. *Soft Matter* **15**, 785–791 (2019).

36. Choi, G. H. et al. Ag nanoparticle/polydopamine-coated inverse opals as highly efficient catalytic membranes. *ACS Appl. Mater. Interfaces* **8**, 3250–3257 (2016).

37. Ejima, H. et al. One-step assembly of coordination complexes for versatile film and particle engineering. *Science* **341**, 154–157 (2013).

38. Liang, Y. et al. Universal quinone electrodes for long cycle life aqueous rechargeable batteries. *Nat. Mater.* **16**, 841–848 (2017).

39. Guo, J. et al. Engineering multifunctional capsules through the assembly of metal–phenolic networks. *Angew. Chem. Int. Ed.* **53**, 5546–5551 (2014).

40. Liu, T. et al. Self-polymerized dopamine as an organic cathode for Li- and Na-ion batteries. *Energy Environ. Sci.* **10**, 205–215 (2017).

41. Deng, Y. et al. Durable polydopamine-coated porous sulfur core–shell cathode for high performance lithium–sulfur batteries. *J. Power Sources* **300**, 386–394 (2015).

42. Alfieri, M. L. et al. The chemistry of polydopamine film formation: The amine-quinone interplay. *Biomimetics* **3**, 26 (2018).

43. Spotnitz, R. Simulation of capacity fade in lithium-ion batteries. *J. Power Sources* **113**, 72–80 (2003).

44. Seo, J., Hyun, S., Moon, J., Lee, J. Y. & Kim, C. High performance of a polydopamine-coated graphite anode with a stable SEI layer. *ACS Appl. Energy Mater* **5**, 5610–5616 (2022).

45. Zinth, V. et al. Inhomogeneity and relaxation phenomena in the graphite anode of a lithium-ion battery probed by in situ neutron diffraction. *J. Power Sources* **361**, 54–60 (2017).

46. Kim, J., Park, S., Hwang, S. & Yoon, W.-S. Principles and applications of galvanostatic intermittent titration technique for lithium-ion batteries. *J. Electrochem. Sci. Technol* **13**, 19–31 (2022).

47. Beattie, S. D. et al. Understanding capacity fade in silicon based electrodes for lithium-ion batteries using three electrode cells and upper cut-off voltage studies. *J. Power Sources* **302**, 426–430 (2016).

48. Yoon, T., Nguyen, C. C., Seo, D. M. & Lucht, B. L. Capacity fading mechanisms of silicon nanoparticle negative electrodes for lithium ion batteries. *J. Electrochem. Soc.* **162**, A2325–A2330 (2015).

49. Tatara, R. et al. The effect of electrode-electrolyte interface on the electrochemical impedance spectra for positive electrode in Li-ion battery. *J. Electrochem. Soc.* **166**, A5090–A5098 (2019).

Acknowledgements

Author contributions

M.G.N. and P.J.Y. conceived the system and established the ELET theory including design of testing condition and related mathematical expressions. M.G.N. carried out the main experiments and relevant anaylses. H.J.S. provided major participation for sample preparation. G.H.C. carried out electrochemical impedance spectroscopic measurements. J.K.K and Y.-J.K conducted pouch cell tests. Y.S.K., H.J.K., C.S.S., Y.K., J.H.N. and H.C. verified the reproducibility of ELET results with the facilities in Samsung SDI Co., Ltd. M.G.N and P.J.Y. wrote the paper and discussed the results.

Competing interests

The authors declare no competing interests.

Additional information

Supplementary information The online version contains supplementary material available at https://doi.org/10.1038/s43246-024-00463-x.

Correspondence and requests for materials should be addressed to Pil J. Yoo.

Peer review information *Communications Materials* thanks Sandeep Suresh Sebastian and the other, anonymous, reviewer(s) for their contribution to the peer review of this work. Primary Handling Editors: Jie Xiao and Jet-Sing Lee. A peer review file is available.

Reprints and permissions information is available at http://www.nature.com/reprints

Publisher's note Springer Nature remains neutral with regard to jurisdictional claims in published maps and institutional affiliations.